

1 Importance of considering site effects in earthquake source parameter
2 estimates: Insights from shallow attenuation at a dense array in
3 Oklahoma

4 Hilary Chang¹ , Rachel E. Abercrombie² , and Nori Nakata^{1,3} 

ABSTRACT

Separating propagation effects from earthquake spectra for source characterization is not a trivial task. The propagation effect contains a site-dependent term in the shallow sediments that absorb high-frequency energy and cause narrow-band amplifications. Neglecting potential site effects can cause large bias and station-wise scattering in corner frequency (f_c) estimates, resulting in significant stress drop deviation. In this study, we investigate shallow attenuation at the LArge-n Seismic Survey in Oklahoma (LASSO) and potential site effects in source parameter measurements due to simplified attenuation models. The high frequency site attenuation parameter kappa (κ_0) of regional earthquakes suggests that attenuation increases rapidly near the surface. The quality factor estimated by shear waves (Q_s) is 10 – 79 on the upper 400 m and 30 – 224 on the upper 2 km. The surface Quaternary sediments have higher attenuation. With a synthetic test using Brune's model, we find that using a non-site-dependent attenuation model leads to large apparent variability in station-wise f_c measurements due to the non-uniqueness of parameters. The apparent median estimate can significantly deviate from the true value with no indication from model misfits. The variability and bias in the estimated f_c depend on site condition and distance; and the dependencies vary with fitting assumptions. We demonstrate that an apparent scaling relation in a previous study for local microearthquakes ($1.3 < M_w < 3.0$) can be largely removed by adding a site term in the estimation, restricting to sites on the higher Q formations, and limiting the parameter space. This study highlights the utmost importance in considering site effects even in a region with no apparent topography changes.

1. Department of Earth, Atmospheric, and Planetary Sciences, Massachusetts Institute of Technology, Cambridge, Massachusetts, 02139, USA; 2. Department of Earth and Environment, Boston University, Boston, Massachusetts, 02215, USA; 3. Lawrence Berkeley National Laboratory, Berkeley, California, 94720, USA

*Corresponding author: hilarych@mit.edu

Cite this article as Chang, H., R.E. Abercrombie, and N. Nakata (2022). Importance of considering site effects in earthquake source parameter estimates: Insights from shallow attenuation at a dense array in Oklahoma, *Bull. Seismol. Soc. Am.* **XX**, 1–35, doi: [00.0000/0000000000](https://doi.org/10.0000/0000000000).

KEY POINTS

- Attenuation is dominantly site-dependent in the Central United States.
- Site effects introduce large uncertainties and biases with apparently small model misfits.
- Having controlled site conditions is more important than using many stations in estimating source parameters.

Supplemental Material

INTRODUCTION

An earthquake seismogram contains source effects convolving with propagation effects:

$$u(f) = s(f) \cdot p(f) \cdot g(f), \quad (1)$$

where f is frequency, $u(f)$ is particle displacement, velocity, or acceleration spectra. $s(f)$ is the source model. $p(f)$ is the path term that describes the propagation time and path-dependent attenuation. $g(f)$ is the site-dependent term. The site term is associated with, for example, shallow unconsolidated sediments that have higher attenuation and resonance effects. Incorrect separation of the path and site terms can bias measurements of source parameters such as stress drop ([Abercrombie, 1995](#)).

Earthquake stress drop is the change of average stress over the fault and relates to the energy released from the source. The stress drop is an important parameter for understanding source physics, rupture simulation, and ground motion modeling. However, stress drop measurements are highly variable ([Allmann and Shearer, 2009](#); [Cocco et al., 2016](#); [Abercrombie et al., 2016](#); [Oth et al., 2017](#)). The resolution limit for moderate to small events causes deviations in stress drop estimates and apparent breakdowns in

²² earthquake self-similarity ([Abercrombie, 1995, 2021](#)). The recent Community Stress
²³ Drop Validation Project ([Baltay et al., 2024](#)) has revealed highly variable measurements
²⁴ for the 2019 Ridgecrest earthquake sequence among different research teams. They
²⁵ found that the stress drop estimates vary due to methods and assumptions. While many
²⁶ of them observed an increase of stress drops with magnitudes, the observations are still
²⁷ within the range of uncertainty of a constant stress drop. Whether the observed earth-
²⁸ quakes scaling is due to method biases, simplified assumptions, or actual indication of
²⁹ non-self-similarity, is still under debate.

³⁰ One of the biggest uncertainty in stress drop estimates comes from the uncertainty
³¹ in corner frequency (f_c) measurements ([Abercrombie, 2021](#)). Earthquake stress drop
³² for a circular crack can be modeled as ([Eshelby, 1957; Madariaga, 1976](#)):

$$\Delta\sigma = \frac{7}{16} \left(\frac{f_c}{k\beta} \right)^3 m_0, \quad (2)$$

³³ where f_c relates to the source dimension. m_0 is the seismic moment, k is a constant
³⁴ depending on the wave type and the rupture model, and β is the shear-wave velocity
³⁵ at the source focal depth. f_c is highly sensitive to the shape of the earthquake spectra
³⁶ and exhibits a notorious trade-off with site effects ([Anderson, 1986; Boore, 1986; Ko
et al., 2012](#)). The uncertainty in f_c is magnified by the power of three, biasing the cal-
³⁷ culated stress drop and leading to apparent scaling relations between earthquake size
³⁸ and source dimension ([Abercrombie, 1995](#)).

⁴⁰ There are different approaches for separating the source from propagation effects.
⁴¹ The spectral-ratio method assumes co-located small events with the same focal mecha-
⁴² nism can represent Empirical Green's Functions (EGFs) and uses these EGFs to remove

43 propagation effects (Hartzell, 1978; Hough, 1997; Mayeda et al., 2007; Abercrombie,
 44 2015). Large-scale inversion methods, including the Generalized Inversion Technique
 45 (GIT; Andrews, 1986; Castro et al., 1990; Hartzell, 1992; Oth et al., 2011; Bindi
 46 et al., 2020), and spectral decomposition (e.g., Shearer et al., 2006, 2019), derive non-
 47 parametric site response spectra to isolate the source spectra. However, estimated site
 48 effects from spectral decomposition involve considerable uncertainties and are highly
 49 dependent on assumed parameters Shearer et al. (2019); Bindi et al. (2023). Each
 50 method relies on specific assumptions, and the choice of method often depends on
 51 available data.

52 Many approaches use an exponential decay to characterize attenuation in a conven-
 53 tional Brune's spectral model (Brune, 1970; Boatwright, 1978, 1980):

$$\Omega_t(f) = \frac{\Omega_0}{[1 + (f/f_c)^{\gamma n}]^{1/\gamma}} \cdot e^{-\pi f \kappa}, \quad (3)$$

54 where $\Omega_t(f)$ is the earthquake farfield displacement spectra, Ω_0 is the long-period
 55 spectral amplitude, n is the high-frequency fall-off rate, and γ is 1 or 2 depending on
 56 whether using a Brune or Boatwright model. The exponential term characterizes the
 57 propagation effect (Anderson and Hough, 1984). In the following, we refer to spec-
 58 tral fitting using Equation 3 as the single-spectra (fitting) approach. The spectral decay
 59 parameter κ has a unit of seconds to make the power of the exponential term dimen-
 60 sionless. κ integrates travel time (tt_i) divided by quality factor (Q_i) across each layers i
 61 along the propagation path (Hough and Anderson, 1988):

$$\kappa = \int_{path} \frac{tt_i}{Q_i}. \quad (4)$$

⁶² Because the Earth is a 3D heterogeneous structure, different parts of the ray path con-
⁶³ tribute differently to the total κ . Near-surface layers in general have lower Q and can
⁶⁴ dominate the variability of κ . [Abercrombie \(1997\)](#) found that in the Cajon Pass bore-
⁶⁵ hole in California, 90% of the attenuation for earthquakes with an epicentral distance
⁶⁶ under 15 km occurs in the upper 3 km, while half of the attenuation occurs in the upper
⁶⁷ 300 m. In stable tectonic regions such as the Central and Eastern United States (CEUS),
⁶⁸ soft sediments overlay a crust with relatively lower attenuation, and the site term can
⁶⁹ contribute even more significantly to the total attenuation for an earthquake.

⁷⁰ We can never have enough information about the subsurface and always have to
⁷¹ make assumptions. Many studies assume that the attenuation dominantly depends on
⁷² travel times. For example, the single-spectra fitting approaches in [Supino et al. \(2019\)](#)
⁷³ and [Kemna et al. \(2020, 2021\)](#) assumed attenuation is travel time divided by a constant
⁷⁴ Q . This simplification raises concerns because attenuation along the path also depends
⁷⁵ on other factors such as source depth and site condition. For comparing shallow and
⁷⁶ deep earthquakes where the attenuation structures along the propagation paths are
⁷⁷ very different, a source-depth dependent Q is required to model κ ([Abercrombie et al.,](#)
⁷⁸ [2021](#)); otherwise, the simplification can cause apparent scaling relations with depth
⁷⁹ (e.g., [Baltay et al., 2024](#)). For modeling spectra where site attenuation actually dom-
⁸⁰ inates, failing to include a site term can cause parameter trade-offs with unmodeled
⁸¹ attenuation. However, the site-effect-related uncertainties can be difficult to examine
⁸² in real data as we often do not have good enough station coverage to investigate site
⁸³ effects without influences from the source and the path.

84 Here, we use a dense array to investigate the impact of simplified site effects on the
85 uncertainties of source parameters. Our work builds on a series of previous studies in
86 the LArge-n Seismic Survey in Oklahoma (LASSO; Figure 1). [Kemna et al. \(2020\)](#) found
87 local microearthquake source parameters measured by the single-spectra approach
88 showed large variabilities among stations (Figure 1(b)(c)) and a strong scaling relation,
89 which was not seen in their spectral-ratio results. Their fitting approach assumed atten-
90 uation depended solely on travel times. [Chang et al. \(2023\)](#) found local site conditions,
91 despite having relatively flat topography, varied significantly with surficial geology.
92 The Quaternary sediments play an especially important role in site effects. They found
93 source parameters consistently correlate with the estimated site terms, but the calcu-
94 lated corrections could only account for a small fraction of the inter-station variability
95 in corner frequency estimates; the cause of the majority of the large inter-station mea-
96 surement variabilities remain unclear. [Chang et al. \(2024\)](#) further investigated the
97 velocity structure and surface amplification caused by the near-surface formations.
98 In this study, we analyze the near-surface attenuation based on the previous velocity
99 structure study. We use the attenuation information to generate synthetic data, attempt
100 to fit them under different conditions, and compare the results with the real data to
101 understand the variability of source parameters caused by the underlying assumptions.

102 To estimate site attenuation, we measure the high frequency spectral decay parame-
103 ter kappa (κ) using the acceleration spectra of regional earthquakes (κ_{acc}). κ contains
104 a distance dependent (κ_r) and a site-dependant component (κ_0). The later is an impor-
105 tant site parameter in ground motion modeling ([Laurendeau et al., 2013](#); [PEER, 2015](#))
106 and loosely correlates with V_{s30} – the average shear-wave velocity in the top 30 meters

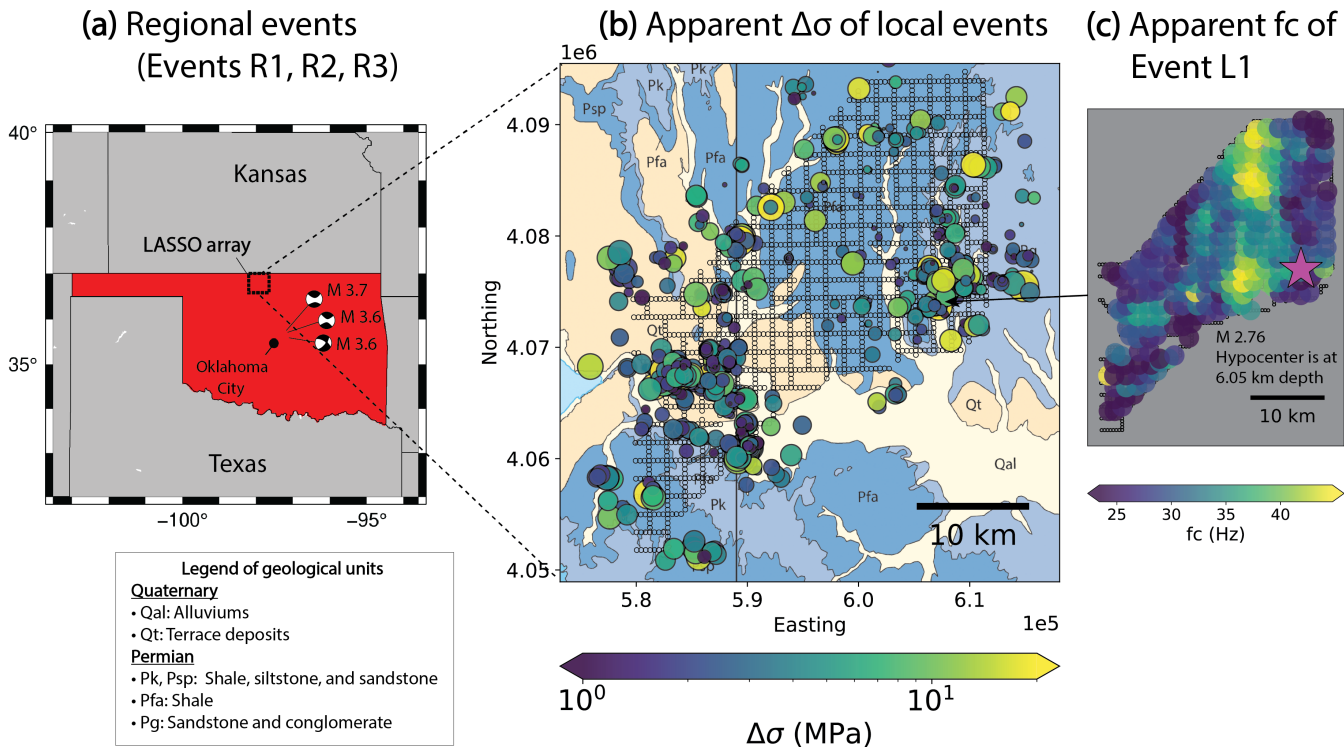


Figure 1: Regional and local earthquakes recorded at the LASSO array and the variability of source parameter measurements using a single-spectra fitting approach. In (a), the focal mechanisms show the three largest regional earthquakes (event R1, R2, R3) that are 126 – 178 km from the array. The small dashed box marks the array location. In (b), the colored circles are local events. The colors indicate apparent stress drop ($\Delta\sigma$) according to the single-spectra measurements in Kemna et al. (2020). The size of the circles is proportional to local magnitudes (0.01–3.0). The small black circles are stations. The map shows the surface geology (see legend on the lower left; Heran et al., 2003). In (c), we show the variability of corner frequency (f_c) estimates for a local event (event L1; the magenta star marks the epicenter). Each colored dot in (c) represents the median f_c measured by a subarray that includes stations within a 2.5 km diameter circle.

107 (Chandler et al., 2006; Ktenidou et al., 2014). While V_{s30} is a proxy for the shear-wave
 108 velocity profile, κ characterizes spectral attenuation and is especially important at rock
 109 and stiff-soil sites ($V_{s30} = 500$ – 1500 m/s; Laurendeau et al., 2013) like those often
 110 found in CEUS. There are many different ways to measure κ and the difference between
 111 methods is larger than the difference between regions (Ktenidou et al., 2014).

112 LASSO ARRAY AND THE DATA

113 The LArge-n Seismic Survey in Oklahoma (LASSO; Dougherty et al., 2019) array con-
 114 tains 1825 stations in an area of 25 km x 32 km. The minimum station spacing is 400
 115 m. The stations are Fairfield Nodal vertical-component 10 Hz nodes with a sampling

rate of 500 Hz. The observed data are proportional to particle velocity. The array was deployed from mid-April to mid-May in 2016 for about a month to investigate local earthquakes associated with wastewater injections. The array recorded more than a thousand of microearthquakes with local magnitudes range from 0.01 to 3.0 with the majority of them occurring at 1.5 – 5.5 km depth (Cochran et al., 2020). The array is on a flat plain in the Anadarko Shelf (Johnson and Luza, 2008). The basin basement is at about 2.2 km depth and tilts gently ($< 1^\circ$) toward the southwest (Crain and Chang, 2018). The topography is flat with a low relief (less than 100 m across the array). The shear-wave velocity structure shows a smooth lateral transition following the basin basement (Chang et al., 2024). The Quaternary sediments within the top 50 m (formations with varying yellows in Figure 1(b); Heran et al., 2003) play an important role in amplifying ground motions (Chang et al., 2023, 2024).

Kemna et al. (2020) used both a single-spectra fitting approach (Equation 3) and a spectral ratio approach to calculate source parameters, including corner frequency (f_c), seismic moment (M_0), and stress drop ($\Delta\sigma$). We focus on their single-spectra f_c measurements. They assumed $\kappa = tt/Q$ in Equation 3, and perform a grid-search to find a combination of $Q = 600$ and $n = 3.5$ yielded the overall best fit. They tried using the Brune model ($\gamma = 1$) and the Boatwright model ($\gamma = 2$) where the latter gives a lower misfit. Chang et al. (2023) found those f_c measurements in individual events to have consistent spatial preferences (Figure 1(c)). The apparent stress drops calculated based on these corner frequencies show lower values on Quaternary sediments (Figure 1(b)). We aim to further understand how site effects contribute to the bias and how to improve the measurements.

139 The array recorded 14 regional earthquakes with local magnitudes range from 3.0 to
140 3.7 from Central Oklahoma (126 – 240 km away; Table S2; [U.S. Geological Survey](#)). We
141 focus on the largest 3 events (R1 – R3, 126 – 178 km away from the array; labeled in
142 Figure 1(a)) to analyze the high-frequency attenuation parameter from their acceler-
143 ation spectra (κ_{acc}). We compare the site component of κ_{acc} with the median ground
144 motions of these 14 regional events. The ground motions are the Root-Mean-Square
145 (RMS) amplitude of particle velocity during P and S arrivals from [Chang et al. \(2023\)](#).
146 Previous studies have found that the ground motions of these regional events are
147 strongly influenced by Quaternary sediments ([Chang et al., 2023, 2024](#)).

148 We group the stations into 272 subarrays. Each subarray consists of stations within a
149 circle of 2.5 km diameter (15 – 20 stations). We stack spectra in each subarray and take
150 the median ground motion measurements and median f_c measurements from [Kemna
151 et al. \(2020\)](#) among the stations in a subarray. In the following analysis, the spectra and
152 data points in the figures represent subarrays instead of individual stations.

153 SHALLOW ATTENUATION ACROSS THE LASSO ARRAY

154 We estimate the high-frequency spectral decay parameter κ_{acc} on the acceleration
155 spectra based on [Anderson and Hough \(1984\)](#):

$$\kappa_{acc} = -\frac{1}{\pi} \frac{d(\ln(A))}{df}, \quad (5)$$

156 where $\frac{d(\ln(A))}{df}$ is the slope of the acceleration spectrum in linear-log space and has a unit
157 of second. The measured κ_{acc} has a site-dependent component $\kappa_{0,acc}$ and a distance-
158 dependent component $\kappa_{r,acc}$. The site component $\kappa_{0,acc}$ can be derived by removing a
159 linear dependence between κ_{acc} and epicentral distances ([Ktenidou et al., 2015](#)).

¹⁶⁰ We use three regional earthquakes in Central Oklahoma (local magnitude $M_L = 3.6 -$
¹⁶¹ 3.7; R1 – R3 in Table S2) to estimate $\kappa_{p,acc}$ for P arrivals and $\kappa_{s,acc}$ for S arrivals (Figure
¹⁶² 2). Data pre-processing includes demeaning, detrending, removing the instrument
¹⁶³ response from the raw data, and convert the particle velocity to particle acceleration.
¹⁶⁴ We calculate the acceleration spectra in a 1.5 s window around the P and S arrivals. We
¹⁶⁵ use a short time window to avoid scattering effects that can result in an underestimated
¹⁶⁶ attenuation (PEER, 2015). We discard data points where the signal-to-noise ratio (SNR)
¹⁶⁷ is under 3. The SNR is defined to be the ratio between the spectral amplitude of the sig-
¹⁶⁸ nal to that of the noise, which is calculated in a 1.5 s window, 8 s before the P arrivals.
¹⁶⁹ We measure the slope on the remaining acceleration spectra above 15 Hz, where the
¹⁷⁰ slope appears to be consistent. The source dimension effect is minimal as events R1 –
¹⁷¹ R3 have corner frequencies much lower than 15 Hz (about 2 – 5 Hz, estimated from
¹⁷² spectral fitting). We require the minimum frequency range of the measurement to be
¹⁷³ > 8 Hz. The SNR and frequency range requirements follow suggestions in Ktenidou
¹⁷⁴ et al. (2016).

¹⁷⁵ The spectral-attenuation parameters $\kappa_{p,acc}$ and $\kappa_{s,acc}$ show strong site-dependence
¹⁷⁶ (Figure 3). The Quaternary formations in general have a higher $\kappa_{p,acc}$ and $\kappa_{s,acc}$. Sites
¹⁷⁷ with higher $\kappa_{s,acc}$ also tend to have higher $\kappa_{p,acc}$. The highest $\kappa_{p,acc}$ corresponds to
¹⁷⁸ rivers and streams. For regional event R1, R2, and R3, $\kappa_{s,acc}$ of ranges from 0.0067 –
¹⁷⁹ 0.041 s while $\kappa_{p,acc}$ spans a wider range with a few unexpected negative values (-0.0051
¹⁸⁰ – 0.084 s) (Figure 3(c)). The measured absolute values of $\kappa_{p,acc}$ and $\kappa_{s,acc}$ contain not
¹⁸¹ only attenuation effect but also a high-frequency amplification effect due to crustal pro-
¹⁸² files in the Central US (Boore and Joyner, 1997; Figure 2 in Campbell and Bozorgnia,

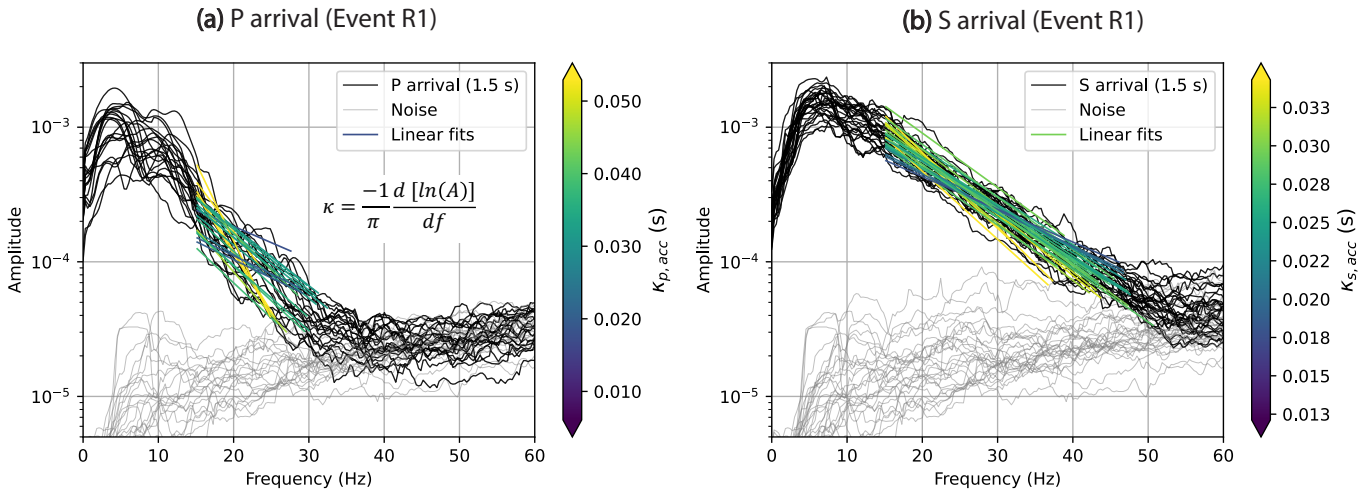


Figure 2: Spectral decay parameters measured from the acceleration spectra of regional event R1. **(a)** P-arrival for $\kappa_{p,acc}$, and **(b)** S-arrival for $\kappa_{s,acc}$. Each spectrum is stacked among stations within a subarray of a 2.5 km diameter circle (15 – 20 stations). The black and grey curves represent signals and noises. The signal spectra are calculated in a 1.5 s window around the P- or S-arrivals. The noise spectra are calculated in a 1.5 s window that is 8 s before the P arrivals.

183 2014). As $\kappa_{p,acc}$ positively correlates with $\kappa_{s,acc}$, but the latter has a much lower uncer-
 184 tainty, we use $\kappa_{s,acc}$ to characterize site attenuation in the following analysis. This
 185 gives more conservative results as $\kappa_{s,acc}$ spans a smaller range. We repeat the analysis
 186 using $\kappa_{p,acc}$ but find $\kappa_{s,acc}$ gives a better results possibly due to the better measurement
 187 quality.

188 Assuming the source effect is negligible at high frequency (> 15 Hz here), κ repre-
 189 sents the propagation effects and is consisted of a path component ($\kappa_r(r)$) and a site
 190 component (κ_0) (Ktenidou et al., 2015):

$$\kappa \approx \kappa_r(r) + \kappa_0. \quad (6)$$

191 Here, r represents the epicentral distance. We can obtain the site term after remov-
 192 ing the distance-dependent $\kappa_r(r)$. We do not observe a clear relationship of increasing
 193 attenuation with increasing epicentral distances between measurements due to the
 194 large variabilities in κ measurements (Figure S1). According to Ktenidou et al. (2016),

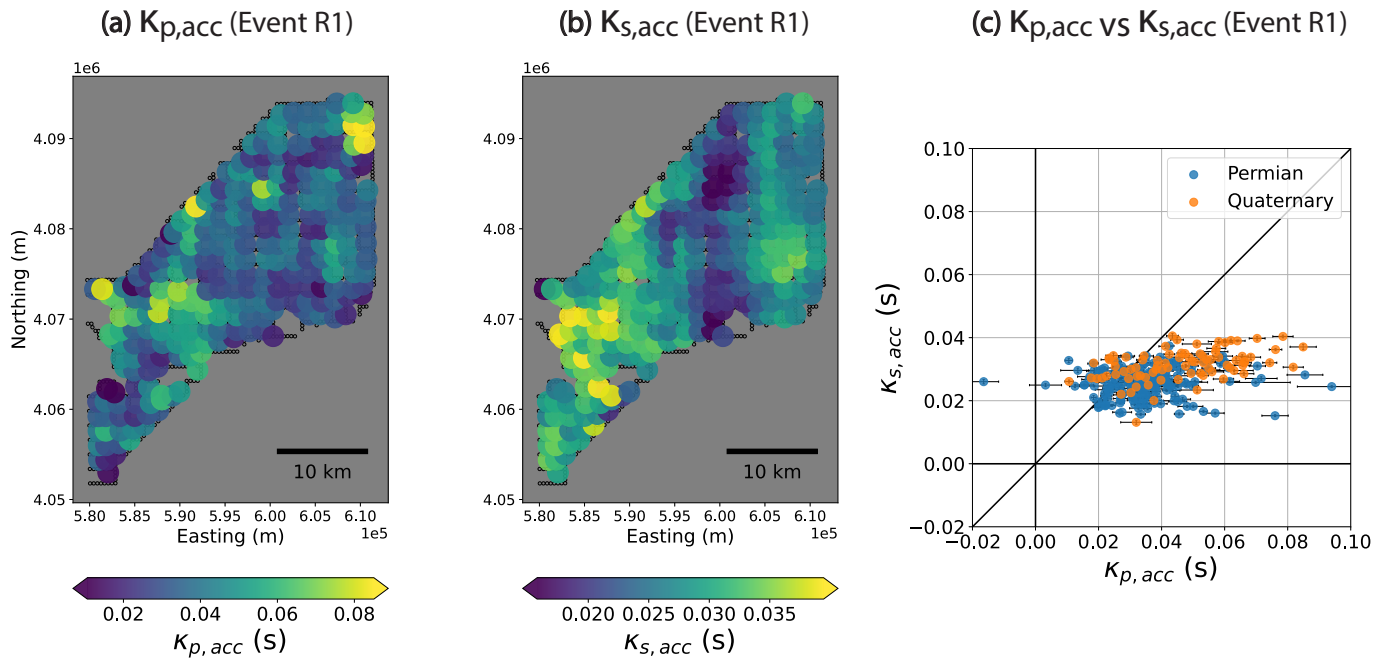


Figure 3: Comparing the spectral decay parameters (a) $\kappa_{p,acc}$ and (b) $\kappa_{s,acc}$, and (c) $\kappa_{p,acc}$ vs $\kappa_{s,acc}$ for regional event R1. In (a) and (b), each colored circle represents a subarray consisting of stations within a 2.5 km diameter circle (15 – 20 stations; small black circles in the background). The color ranges are cut at 1% and 99% of the total range for visualization. The dots in (c) are colored by the dominant type of superficial geology of the subarray. The error bars are the standard deviation of the fitting. The uncertainties for $\kappa_{s,acc}$ (vertical error bars; most are hidden behind the dots) are much lower than that for $\kappa_{p,acc}$ (horizontal error bars).

195 a distance of 50 – 100 km is necessary to observe the κ -distance relation in the CEUS,
 196 where the crust has low attenuation. Nonetheless, the total epicentral distance is more
 197 than 120 km, which is sufficient to resolve the path dependence. We assume the path
 198 term is nearly constant across the array and the path term is represented by the mini-
 199 mum $\kappa_{s,acc}$ of the three events (i.e., $\min(\kappa_{s,acc}) = \kappa_r$). We estimate the site term $\kappa_{0,s,acc}$
 200 by subtracting $\min(\kappa_{s,acc})$ from $\kappa_{s,acc}$. The resulting $\kappa_{0,s,acc}$ ranges from 0.0036 to 0.0286
 201 S.

202 Figure 4(a) shows that $\kappa_{0,s,acc}$ positively correlates with the median ground motions
 203 of regional earthquakes from Central Oklahoma. Note that ground motions in the P-
 204 wave window at 2 – 4 Hz have an opposite trend due to the radiation pattern (Chang

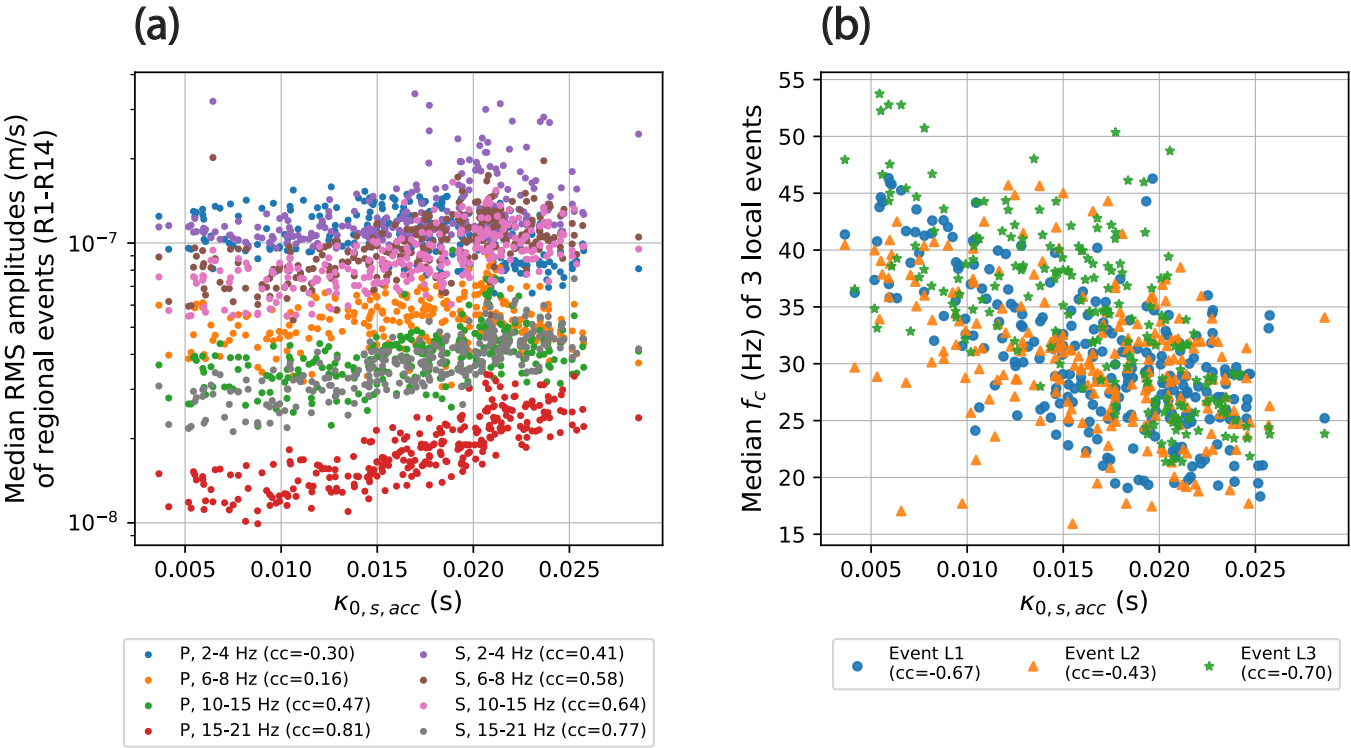


Figure 4: Site spectral decay parameter $\kappa_{0,s,acc}$ correlates with (a) median ground motions of regional earthquakes and (b) station-wise corner frequency (f_c) measurements of 3 local earthquakes (L1 – L3, Table S1). Ground motions in (a) are the median Root-Mean-Square (RMS) amplitudes of 14 regional earthquakes (Table S2). Colors indicate time windows and frequency ranges of the RMS amplitudes (P wave: -1 – 10 s and S wave: 10 – 30 s relative to P arrivals). Each f_c data point in (b) is the median measurements among stations within a subarray, where the f_c measurements at stations are from Kemna et al. (2020). cc denotes the cross-correlation coefficient. All non-zero cc values shown in the plot have p-values < 5%.

et al., 2023). $\kappa_{0,s,acc}$ negatively correlates with station-wise f_c measurements of local earthquakes (Figure 4(b)).

The S-wave quality factor Q_s is related to $\kappa_{0,s,acc}$ via travel time according to Equation 4. Assuming the site term associates with structure in the top H meters, we have:

$$Q_s = \frac{\sum_{i=0}^{i=H} tt_i}{\kappa_{0,s,acc}}. \quad (7)$$

Here, we obtain the travel time via the shear-wave velocity structure under the array from Chang et al. (2024). The velocity profiles consist of nearly horizontal layers with gentle tilting ($< 1^\circ$). There are roughly four known interfaces that possibly capture characteristics of site-varying attenuation. These interfaces are at the following depths:

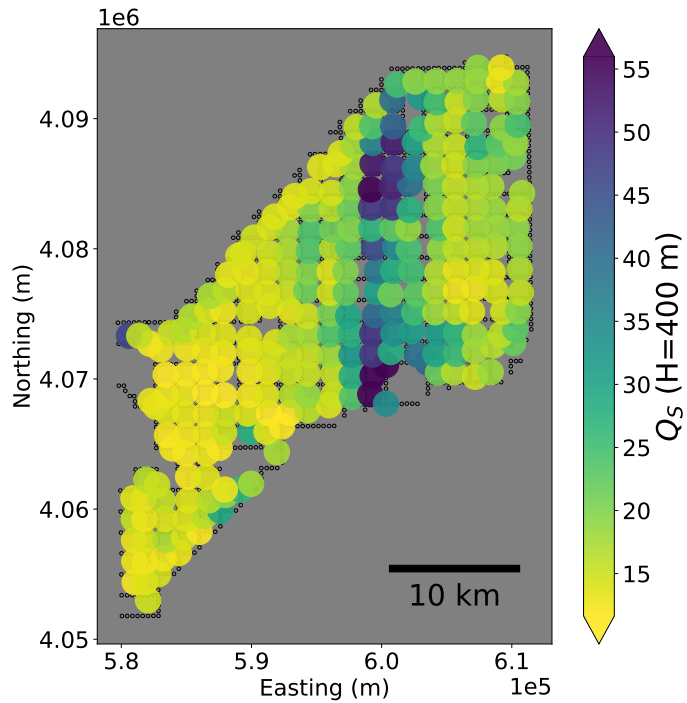


Figure 5: Map of S-wave quality factor (Q_s) in the top 400 m derived from the site spectral decay parameter $\kappa_{0,s,acc}$ and the shear-wave velocity structure. Each colored circle represents a subarray consisting of stations within a 2.5 km diameter circle (15 – 20 stations; small black circles in the background). The color ranges are cut at 1% and 99% of the total range for visualization. The total range of Q_s is 10 – 79.

(1) few to tens of meters, (2) ~ 300 m, (3) ~ 1.2 km, and (4) ~ 2.2 km, associated with (1) a strong impedance contrast between Quaternary sediments and Permian sandstones, (2) and (3): rapid velocity transitions, and (4) basin basement, respectively.

We assume $H = 400$ m which give a Q_s range of 10 – 79 in the top 400 m (Figure 5). Assuming $H = 2000$ m results in $Q_s = 30 – 224$. Different assumptions for H shift the range of Q_s but do not significantly alter the pattern (Figure S2) because the lateral variation of V_s (and therefore variation of travel time in Equation 7) remains relatively constant in the top 2 km. Whether H is 100 m or 2 km, the measured Q_s indicates strong attenuation with considerable variability near the surface. We note that because the velocity model derived from ambient noise lacks good resolution in the upper 50 m and may have higher-than-actual velocity above 50 m, the Q_s we get is a lower bound.

224 Below, we assume $Q_{site} = Q_s$ represents site attenuation at each subarray associated
 225 with the top 400 m for both P and S waves. This is a conservative estimate for the range
 226 of Q_p as $\kappa_{p,acc}$ estimates involve fewer events and span a wider range (Figure 3(c)).
 227 However, we note that Q_p is expected to be higher than Q_s and the variation of Q_p/Q_s
 228 can be affected by saturation states (Winkler and Nur, 1982; Clouser and Langston,
 229 1991; Parolai et al., 2022). We do not address the difference between Q_p and Q_s in this
 230 study.

231 EFFECTS OF IGNORING SITE EFFECTS IN THE SPECTRAL MODEL

232 To investigate the effect of ignoring site-related attenuation, we first generate synthetic
 233 spectra for a local earthquake (event L1) using the site attenuation map we obtained in
 234 the previous section. The synthetic spectra are generated using Equation 3 with $f_c =$
 235 30.0 Hz, $\gamma = 2$, $n = 2.0\text{m}$, and an arbitrary low-frequency amplitude level of $\Omega_0 = 10$.
 236 The attenuation parameter κ for each subarray is formulated as:

$$\kappa \approx \frac{tt}{Q_{path}} + \frac{\sum_{i=0}^{i=m} tt_i}{Q_{site}}, \quad (8)$$

237 , where $\frac{tt}{Q_{path}}$ is path term, assumed to be the total travel time tt from the source to the
 238 middle of the subarray divided by Q_{path} . We calculate the travel time with the Eikonal
 239 equation (White et al., 2020) using the pseudo-3D velocity structure from Chang et al.
 240 (2024) and use $Q_{path} = 1000$ to generate the synthetic spectra. Note that the usage of a
 241 single Q_{path} without a source-depth dependence can be an over-simplification for real
 242 earthquakes, but we will focus on the difference in sites and will not address potential
 243 issues raised due to difference in Q_{path} here as the earthquakes are all relatively shallow
 244 (see Discussions). $\frac{\sum_{i=0}^{i=m} tt_i}{Q_{site}}$ is the site term and is the sum of travel time spent in the top

TABLE 1 : Fitting conditions for P or S wave synthetic spectra of event L1 compared with Kemna et al. (2020). The synthetic spectra assume (1) same Q_{site} for P and S waves, and (2) P wave velocity is 1.78 times the S wave velocity. Apparent f_c is the median of good measurements (<5% uncertainty). The true f_c in synthetic test 1 – test 5 is 30.0 Hz.

Name	P or S spectra	Attenuation model	Assumed Q and n	Dependent variables	$\frac{\text{Apparent } f_c}{\text{True } f_c}$
Kemna et al. (2020)	P	$\kappa = \kappa_{path}$	$Q_{total} = 600, n = 3.5$ (best fit)	$Q_{total}, n, \gamma, f_c$?
Synthetic test 1	P	$\kappa = \kappa_{path} + \kappa_{site}$	$Q_{path} = 350, n = 2.0$ (best fit)	$Q_{path}, Q_{site}, n, f_c$	100%
Synthetic test 2	P	$\kappa = \kappa_{path}$	$Q_{total} = 240, n = 2.0$ (best fit)	Q_{total}, n, f_c	98%
Synthetic test 3	P	$\kappa = \kappa_{path}$	$Q_{total} = 600, n = 3.5$	f_c	87%
Synthetic test 4	S	$\kappa = \kappa_{path}$	$Q_{total} = 260, n = 2.5$ (best fit)	Q_{total}, n, f_c	93%
Synthetic test 5	S	$\kappa = \kappa_{path}$	$Q_{total} = 600, n = 3.5$	f_c	63%

²⁴⁵ $H = 400$ meters divided by the site-specific Q_{site} . There are a total of m layers in the top
²⁴⁶ H meters and we obtain the travel time spent in each layer tt_i by doing ray-tracking in
²⁴⁷ the velocity model. We generate synthetics P and S wave spectra using the same Q_{site}
²⁴⁸ obtained based on regional earthquakes from the previous section. The only difference
²⁴⁹ between P and S spectra is that the velocity is 1.78 faster for P waves than for S waves
²⁵⁰ when calculating the travel times.

²⁵¹ We fit the synthetic spectra with different attenuation models (Table 1). Synthetic
²⁵² test 1 is a benchmark. We consider the site term in κ by fitting with Equation 8 with
²⁵³ the Brune's model. We allow both f_c and Q_{site} to vary and fix $\gamma = 2$. We perform a
²⁵⁴ grid-search to find the combination of Q_{path} and n that gives the overall best fit for
²⁵⁵ all subarrays. We successfully recover $f_c = 30.0$ Hz and Q_{site} at all subarrays for these
²⁵⁶ ideal spectra.

²⁵⁷ In synthetic test 2, we ignore the site term in Equation 8 ($\kappa_{site} = 0$). In that case, the
²⁵⁸ path Q equals to the total Q along the path of propagation: $Q_{path} = Q_{total}$. A grid-search
²⁵⁹ finds a combination of $Q_{total} = 240$ and $n = 2.0$ gives the overall best fit (red star in
²⁶⁰ Figure 6). The map of residuals shows the trade-off between Q_{total} and n as spectral
²⁶¹ falloff parameter n tries to compensate for the unmodeled attenuation in the spectra.
²⁶² In synthetic test 3, we assume a combination of higher $Q_{total} = 600$ and higher $n = 3.5$,

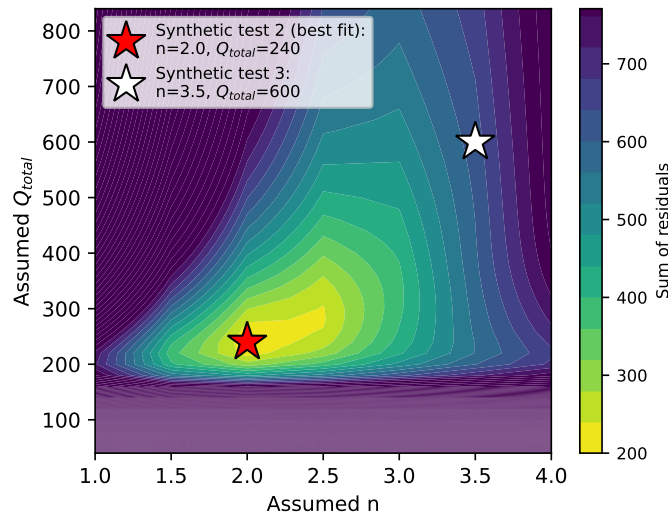


Figure 6: A grid-search in synthetic test 2 that attempts to find a combination of Q_{total} and n to fit the synthetic spectra of event L1. The trade-off between Q and n is apparent. The colors indicate the sum of residuals from fitting the spectra at all subarrays. We perform synthetic test 2 using the best fit at the red star and synthetic test 3 using the combination at the white. Note that the later is the best fit for the real data of event L1 ([Kemna et al., 2020](#)).

which is the best combination found for the actual data of event L1 ([Kemna et al., 2020](#)).

Figure 7 shows the spectral fitting examples in the second and the third synthetic tests. The models seem to fit well with small uncertainties. However, the measured f_c is significantly off from the true $f_c = 30$ Hz. Note that we do not consider site amplification here. With some narrow-banded amplification between 10 and 20 Hz, as suggested by [Chang et al. \(2024\)](#) for sites on the Quaternary formations, the grid-search might find $Q_{total} = 600$ and $n = 3.5$ in Figure 7(b) to fit the spectra better.

Figure 8 shows the highly variable f_c measurements of all subarrays in synthetic tests 2 – test 5. These measurements have fairly good fit with uncertainty less than 5%. However, the apparent f_c scatter across 15 – 90 Hz among subarrays due to the oversimplified attenuation model. Because the actual attenuation involves both the site quality factor (Q_{site}) and travel time (Equation 8), the measured f_c correlates with Q_{site} and the hypocentral distance. However, the large scattering can mask the correlations.

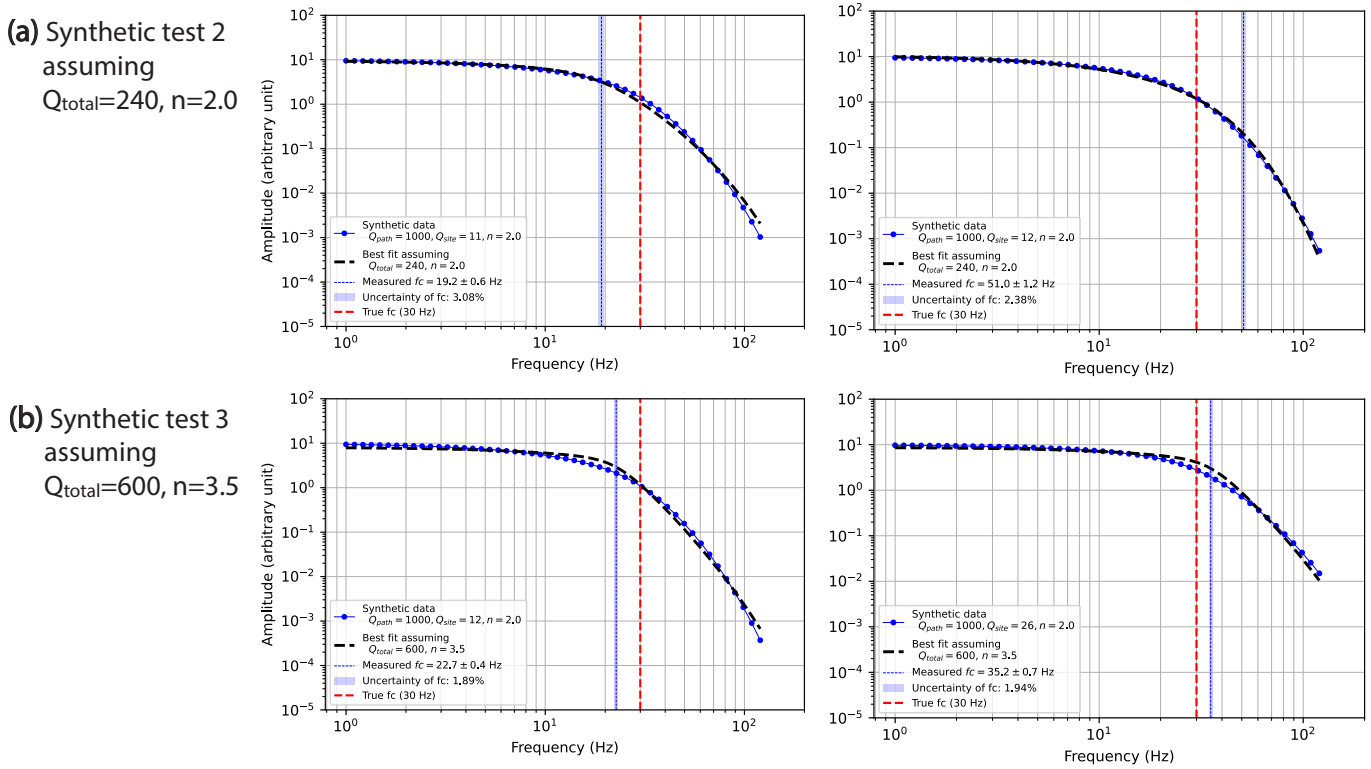


Figure 7: Spectral fitting examples in (a) synthetic test 2, and (a) synthetic test 3. Left and right panels show apparently lower and higher corner frequency (f_c) measurements, respectively for each test. The deviations between the apparent f_c (blue lines) and the true $f_c = 30$ Hz (red lines) are due to an inadequate attenuation model. The blue curves are example synthetic P-wave spectra of event L1 generated with $f_c = 30.0$ Hz, $n = 2.0$, $\gamma = 2.0$, $\Omega_0 = 10$, $Q_{path} = 1000$, and Q_{site} estimated by regional earthquakes. The black curves are the best fits using a constant Q_{total} and a derived n from grid-searching the optimal combination of these two parameters that can best fit all subarrays.

When assuming another set of Q_{total} and n , the apparent relation between f_c and Q_{site} and the hypocentral distance changes (Figure 8(b)). The correlation between f_c and hypocentral distance may not be obvious. Notice that the median f_c deviates from the true f_c . The apparent median f_c can deviate significantly, especially for structures with a lower velocity. In synthetic test 4 and test 5 for the S-wave spectra (Figure 8(c)(d)), the deviation between the apparent and the true f_c is even more severe. We used the same Q_{site} to generate synthetics for P and S wave, so the only difference between simulating P or S-wave spectra is a longer travel time for S waves.

Now, we compare real data of event L1 with the synthetic test results. Kemna et al. (2020) used a similar assumption to our third synthetic test. They assume κ is entirely

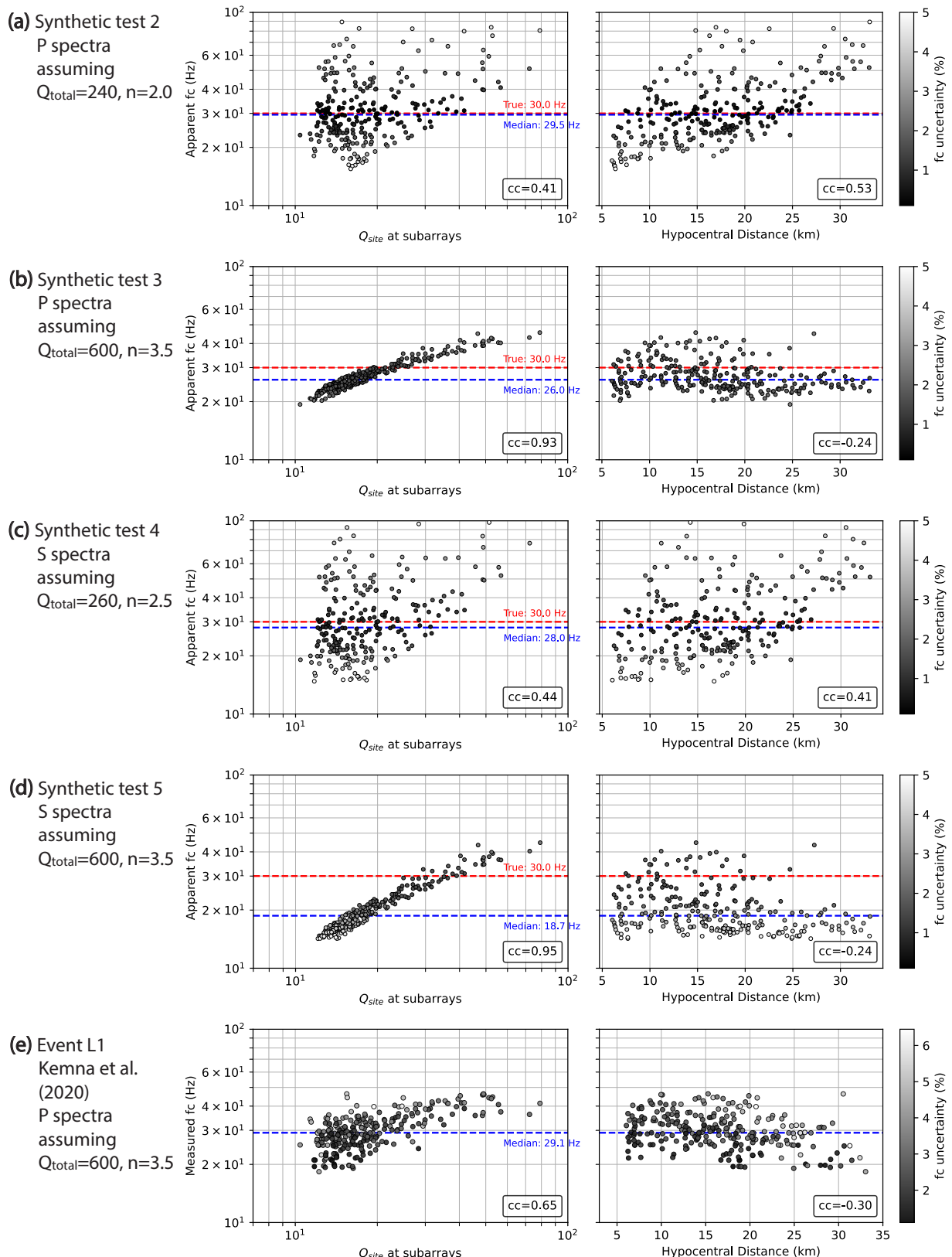


Figure 8: Apparent corner frequency (f_c) of the synthetic P-wave spectra of event L1 in synthetic test 2 – test 5 ((a) – (d)). (e) is the measured f_c from actual data in Kemna et al. (2020). Left: f_c vs the actual Q_{site} used to generate the spectra. Right: f_c vs the hypocentral distance. Red and blue dashed lines are the true f_c and the median of the measurements, respectively. The gray scales indicate fitting uncertainty ((standard deviation of f_c)/ f_c x 100%).

287 travel time dependent and found $Q_{total} = 600$ and $n = 3.5$ fit the overall data the best,
288 possibly due to site amplifications on the Quaternary sites. We observe similar site and
289 distance dependence in their f_c measurements comparing Figure 8(e) with 8(b). The
290 resemblance suggests trade-offs between f_c and Q_{site} , an overestimated n , and possibly
291 a biased f_c overall for this event because of site effects. Other local events also exhibit
292 site dependence (Figure S3, S4).

293 RE-DETERMINING SOURCE PARAMETERS CONSIDERING SITE EFFECTS

294 We re-calculate the source parameters considering site effects for all local events.
295 Different from the single-spectra approach in Kemna et al. (2020) that assumed $\kappa =$
296 κ_{path} , we consider site attenuation with $\kappa = \kappa_{path} + \kappa_{site}$ (Table 2). The site amplification
297 between 8 to 25 Hz on the Quaternary sites (Chang et al., 2023, 2024) can bias the
298 results as we do not consider amplification in our simple model. Hence, we use only
299 Permian sites that have a higher Q_{site} (based on regional earthquakes). Before applying
300 the single-spectra fitting, we perform the following treatment to the data (Text S1).
301 We use a 0.8 s window around the P arrivals to calculate the displacement spectra.
302 We apply a point-wise quality control to discard data points with SNR less than 9. We
303 resample the continuous spectra into a constant interval on the log-frequency scale.
304 We stack the resampled spectra among stations in each subarray.
305 We use Equation 3 to fit the stacked spectra with a fixed $\gamma = 2$ and a fixed $n = 2.0$.
306 We first perform a grid search to determine Q_{path} given $n = 2.0$. In refit tests 1 and 2,
307 we determine both f_c and Q_{site} . In refit test 3, we fix Q_{site} at the values determined
308 from regional events and only determine f_c . Refit test 1 imposes a looser site selection
309 criterion so that we can examine the site dependence. Refit test 2 and 3 have a more

TABLE 2 : Fitting conditions for determining source parameters of LASSO local events.

Name	Attenuation model	Site selection criteria	Assume	Dependent variables
Kemna et al. (2020)	$\kappa = \kappa_{path}$	Permian + Quaternary sites	-	$Q_{total}, n, \gamma, f_c$
Refit test 1	$\kappa = \kappa_{path} + \kappa_{site}$	Permian sites with $Q_{site} > 32$	$n = 2.0, \gamma = 2$	Q_{path}, f_c, Q_{site}
Refit test 2	$\kappa = \kappa_{path} + \kappa_{site}$	Permian sites with $Q_{site} > 44$	$n = 2.0, \gamma = 2$	Q_{path}, f_c, Q_{site}
Refit test 3	$\kappa = \kappa_{path} + \kappa_{site}$	Permian sites with $Q_{site} > 44$	$n = 2.0, \gamma = 2, Q_{site}$	Q_{path}, f_c

strict site selection requirement to examine potential scaling relation of source parameters. In refit test 3, fixing Q_{site} reduces the degree of freedom so that we can reduce the uncertainty and obtain more results that pass the quality control. We require an uncertainty of f_c to be less than 20% for all tests. After getting the median f_c among all subarrays for an event, we calculate the stress drop using Equation 2. We use β based on source depth and the velocity structure (Rubinstein et al., 2018) and use the same $k = 0.38$ assumption and the same seismic moment (m_0) in Kemna et al. (2020) for comparison with their results. We calculate moment magnitude (M_w) using Hanks and Kanamori (1979).

Figure 9 shows the re-calculated f_c for event 1 in refit test 1. These individual high Q sites now get lower f_c values compared to originally (Figure 8(e)), suggesting that f_c were over-estimated at these stiff sites. The median f_c is slightly higher for this event after the recalculation (29.1 Hz before to 31.2 Hz now). The site and distance dependence are not obvious for these stiff sites in general (Figure S3, S4). Although it is more difficult to observe correlations behind the large variation of f_c in this narrow range of site conditions and distances.

In Figure 10(a), the original single-spectra results in Kemna et al. (2020) show a strong scaling relation where smaller events deviate from the lines of constant stress drops. The apparent scaling relation is likely associated with site effects, where small events typically with higher corner frequency are more susceptible to attenuation-

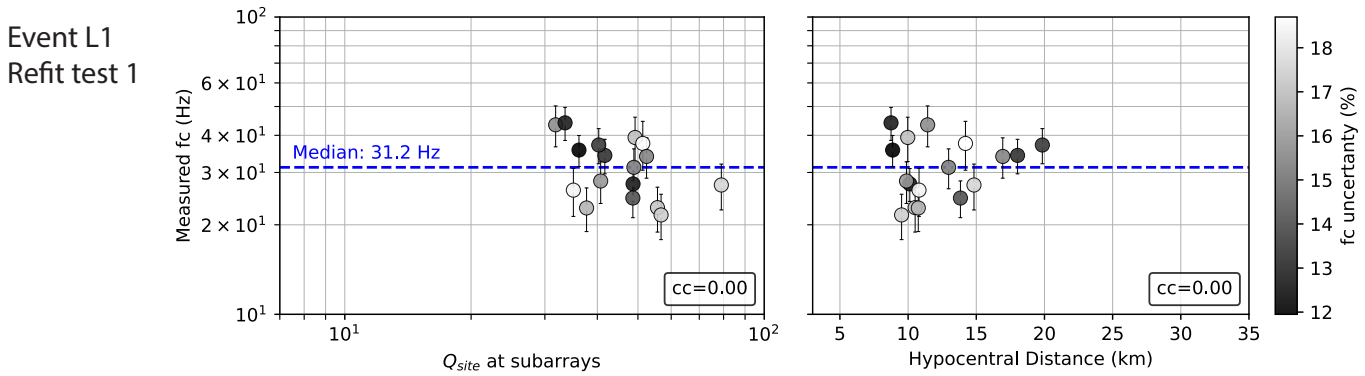


Figure 9: Measured corner frequency (f_c) of event L1 in refit test 1. Left: f_c vs Q_{site} . Right: f_c vs hypocentral distance. We restrict to sites with higher Q_{site} values and hence there are fewer data points compared to Figure 8(e). The gray scales indicate fitting uncertainty (standard deviation of f_c)/ $f_c \times 100\%$). The error bars indicate standard deviation. The blue dashed lines are the median f_c . Each point represents a subarray with 15 – 20 stations within a 2.5 km diameter circle.

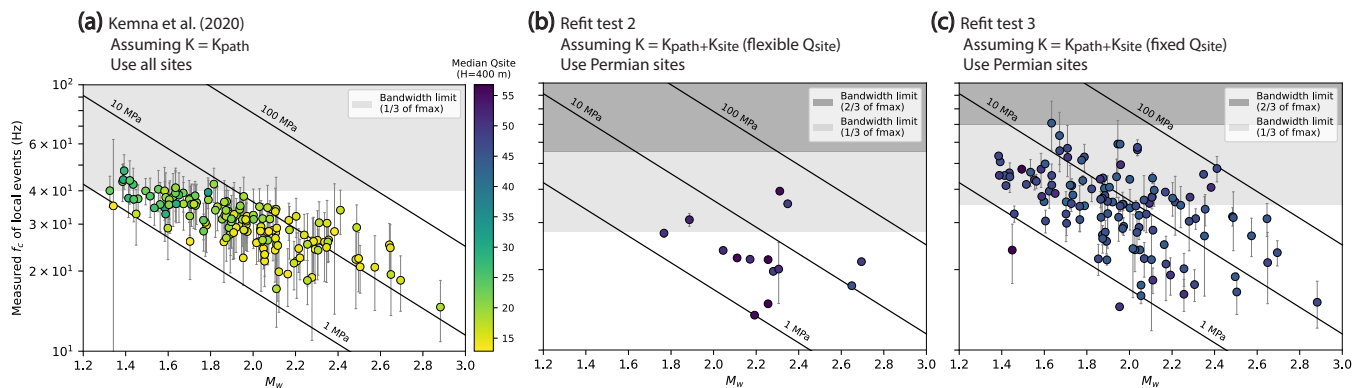


Figure 10: Apparent scaling relation between corner frequency (f_c) and moment magnitude (M_w) in (a) Kemna et al. (2020), (b) refit test 2, and (c) refit test 3. Each dot is the median of an event (among subarrays) with error bars indicating the standard deviation of f_c . The colors indicate the median Q_{site} of subarrays involved in the measurements. The black lines are constant stress drops at 1, 10, and 100 MPa. The shades indicate approximate upper bandwidth limits defined as one and two third of the maximum available frequency of the stacked spectra at subarrays.

related trade-offs. The colors in Figure 10(a) show that smaller events have higher median Q_{site} , likely because they are more likely being ignored by sites with a lower Q . This can cause another selection bias. In the re-calculated results (refit test 2 and 3; Figure 10(b)(c)), where we use only the stiff sites and consider site effects, the source parameters do not exhibit obvious scaling relations.

335 **DISCUSSIONS**

336 **Shallow attenuation and implications of site effects on spectral fitting**

337 The high-frequency decay of the regional earthquakes reveals that Q decreases rapidly
338 near the surface. We find $Q = 10 - 79$ in the upper 300 m and 30 – 224 in the upper 2
339 km. Compared to [Abercrombie \(1997\)](#), which found $Q_s \approx 15$ in the upper 300 m and
340 $\approx 21 \pm 7$ in the upper 2.9 km at Cajon Pass in California, the intra-plate tectonic region
341 of the Central US has highly attenuating shallow sediments overlying stiffer forma-
342 tions. The attenuation is highly site-dependent, and the surface Quaternary sediments
343 have an especially low Q . Assuming a dominantly travel-time-dependent attenuation
344 in Brune's model would cause the apparent corner frequency to vary from site-to-
345 site and bias overall measurements with apparent good fits to the spectra (Figure 7).
346 Moreover, the apparent relation between f_c estimates and distances can be unobvious
347 depending on fitting assumptions (Figures 8). A small correlation between f_c and dis-
348 tance or f_c and travel time does not suggest little influence of site effects. The apparent
349 n values tend to be larger to compensate for the unmodeled site-attenuation that is
350 independent of the total travel time.

351 **Methods to reduce bias and uncertainty in source parameters caused by site effects**

352 We demonstrate that by adding a site-attenuation term, restricting spectral fitting
353 to sites with lower amplification, and limiting the parameter space, we can signifi-
354 cantly reduce the apparent scaling relation (Figure 10). [Kemna et al. \(2020\)](#) and [Chang](#)
355 [et al. \(2023\)](#) also showed that the source parameters estimated using the spectral-ratio
356 approach do not exhibit an apparent scaling relation or correlations with site condi-
357 tions. Although the spectral-ratio methods involve other uncertainties ([Abercrombie](#),

358 2015), and the limited EGF availability for small events can introduce other selection
359 biases, this issue is outside the scope of this study. We also attempted deriving non-
360 parametric site response spectra for correction using regional earthquakes. However,
361 because the regional earthquake have limited SNR above 30 Hz due to attenuation
362 (Figure S5), we could not get reliable f_c measurements from the corrected spectra.

363 Chang et al. (2023) attempted to correct site effects in the source parameter measure-
364 ments by removing a linear trend between site amplification and f_c and m_0 . However,
365 their trend removal is based on the median of station-wise measurements in individual
366 events. Nevertheless, because the median can deviate from the true value (Figure 8),
367 such median-based correction underestimates the event-wise bias due to site effects.
368 On the other hand, one might attempt to find a site-specific scaling factor to correct f_c .
369 However, because the scattering and biases not only relate to the site condition (Q_{site})
370 but also to the source-station configuration, and the fitting assumptions, finding a site
371 specific correction is impossible. Depending on the fitting assumptions, the apparent
372 f_c can have different apparent relations with site conditions and distance. Once the
373 measurements are made, correcting the measurements is not easier than re-doing the
374 fitting under a more adequate assumption.

375 Other potential factors

376 Although not included in our simple model, site amplification is also an important
377 factor to consider. Site amplification on the Quaternary formations creates resonance
378 peaks between 8 – 25 Hz and can reach amplitudes that are 3 – 4 times higher locally
379 (Chang et al., 2023, 2024, Figure S5). If we include Quaternary sites in refit test 1
380 and test 2, the inverted Q_{site} would be completely opposite to what we expected from

³⁸¹ regional earthquakes, and the amplification between 10 – 15 Hz drives the apparent f_c .
³⁸² Chang et al. (2023) also found that ground motions of regional earthquakes at 10 – 15
³⁸³ Hz correlate with f_c the most compared to other frequency bands. Hence, it is impor-
³⁸⁴ tant to select stiff sites to minimize trade-offs due to narrow-banded amplification that
³⁸⁵ is not considered in the simple model.

³⁸⁶ There is a simplification in our attenuation model, which is the usage of a single path-
³⁸⁷ dependent attenuation Q_{path} in Equation 8. In reality, because of the Earth's layered
³⁸⁸ structure, for two earthquakes with the same hypocentral distance, the one directly
³⁸⁹ beneath the station, and thus at a deeper depth, can experience very different atten-
³⁹⁰ uation compared to the one at shallower depth. Using the same Q_{path} to characterize
³⁹¹ both earthquakes causes an apparent scaling relation with increasing source depth
³⁹² (Abercrombie et al., 2021). Baltay et al. (2024) observed that stress drops estimated
³⁹³ without considering source-depth dependent attenuation exhibit stronger correlation
³⁹⁴ with source depths. Because the depths of local earthquakes are all relatively shallow
³⁹⁵ (1.5 km – 5.5 km), the ray paths to most of the stations spend significant times trav-
³⁹⁶ eling in nearly-horizontal layers; hence, a purely travel-time dependent Q_{path} may be
³⁹⁷ sufficient. However, we note that a depth-dependent Q_{path} is required when analyzing
³⁹⁸ earthquakes with greater depths.

³⁹⁹ CONCLUSION

⁴⁰⁰ We use the regional earthquakes ($M_L = 3.6 – 3.7$) to investigate shallow attenuation
⁴⁰¹ at the LArge-n Seismic Survey in Oklahoma (LASSO) and the impact of ignoring
⁴⁰² site effects when fitting with the Brune's source model for local microearthquakes
⁴⁰³ ($1.3 < M_w < 3.0$). Despite the study region having a flat topography, the near-surface

404 attenuation varies significantly. The Quaternary sediments have the lowest Q . The vari-
405 ability of apparent site attenuation is larger than the total amount of path attenuation
406 from earthquakes that are over 120 km away. The P and S wave spectra of regional
407 earthquakes show Q_p and Q_s decreasing rapidly in the near surface. In the top 2 km Q_s
408 ranges 30 to 224, and in the top 400 m, Q_s ranges from 10 to 79.

409 Using synthetic spectra, we demonstrate that mixing stations with different site con-
410 ditions while ignoring site-specific attenuation results in large inter-station variation
411 in apparent corner frequency (f_c) estimates and serious biases between events (Figure
412 8). The impact is more severe for lower-velocity structures. The apparent spectral fall-
413 off parameter n tends to be higher than the true value. The fitting uncertainty fails to
414 account for the scattering and bias because of the non-uniqueness of the model (Figure
415 7). The biased measurements may have little or no apparent correlation with distance
416 depending on fitting assumptions.

417 By adding a site attenuation term and using only sites on stiff formations, we can
418 largely remove the apparent scaling relation between earthquake size and dimension
419 in the single spectra results in Kemna et al. (2020). This study demonstrates the utmost
420 importance of considering site effects even within a simple, flat small region (25 km x
421 32 km). Using a small number of stations with controlled site conditions is more precise
422 and accurate than having a large number of stations with uncontrolled site conditions.

423 DATA AND RESOURCES

424 We use ObsPy (Beyreuther et al., 2010) for earthquake data processing. All spectral fit-
425 tings in Section and are done using LMFIT (Newville et al., 2016). We use PyKonal
426 (White et al., 2020) to calculate travel times in Section and . All data used in this

⁴²⁷ paper came from published sources listed in the references. The supplemental document provides additional supporting information including a detailed description
⁴²⁸ of data processing, supplemental figures, and tables with detailed information of the
⁴²⁹ earthquakes analyzed.
⁴³⁰

⁴³¹ **DECLARATION OF COMPETING INTERESTS**

⁴³² The authors acknowledge there are no conflicts of interest recorded.

⁴³³ **ACKNOWLEDGMENTS**

⁴³⁴ This research was supported by the U.S. Geological Survey under Grant G20AP00022,
⁴³⁵ G20AP00023, G22AP00012, and G22AP00035 to Massachusetts Institute of
⁴³⁶ Technology and Boston University. Nori Nakata is partially supported by the U.S.
⁴³⁷ Department of Energy under Award Number DE-AC02-05CH11231 for this study.

⁴³⁸ **REFERENCES**

- ⁴³⁹ Abercrombie, R. E. (1995). Earthquake source scaling relationships from 1 to 5 M_L using seismograms recorded at 2.5 km depth. *Journal of Geophysical Research: Solid Earth* **100**(B12), 24015–24036.
- ⁴⁴⁰ Abercrombie, R. E. (1997). Near-surface attenuation and site effects from comparison of surface and deep borehole recordings. *Bulletin of the Seismological Society of America* **87**(3), 731–744.
- ⁴⁴¹ Abercrombie, R. E. (2015). Investigating uncertainties in empirical Green's function analysis of earthquake source parameters. *Journal of Geophysical Research: Solid Earth* **120**(6), 4263–4277.
- ⁴⁴² Abercrombie, R. E. (2021). Resolution and uncertainties in estimates of earthquake stress drop and energy release. *Philosophical Transactions of the Royal Society A* **379**(2196), 20200131.
- ⁴⁴³ Abercrombie, R. E., S. Bannister, J. Ristau, and D. Doser (2016). Variability of earthquake stress drop in a subduction setting, the Hikurangi Margin, New Zealand. *Geophysical Journal International*, ggw393.
- ⁴⁴⁴ Abercrombie, R. E., D. T. Trugman, P. M. Shearer, X. Chen, J. Zhang, C. N. Pennington, J. L. Hardebeck, T. H. Goebel, and C. J. Ruhl (2021). Does earthquake stress drop increase with depth in the crust? *Journal of Geophysical Research: Solid Earth* **126**(10), e2021JB022314.
- ⁴⁴⁵ Allmann, B. P. and P. M. Shearer (2009). Global variations of stress drop for moderate to large earthquakes. *Journal of Geophysical Research: Solid Earth* **114**(B1).
- ⁴⁴⁶ Anderson, J. G. (1986). Implication of attenuation for studies of the earthquake source. *Earthquake Source Mechanics* **37**, 311–318.

- 454 Anderson, J. G. and S. E. Hough (1984). A model for the shape of the Fourier amplitude spectrum of acceleration at high frequencies.
455 *Bulletin of the Seismological Society of America* **74**(5), 1969–1993.
- 456 Andrews, D. (1986). Objective determination of source parameters and similarity of earthquakes of different size. *Earthquake source*
457 *mechanics* **37**, 259–267.
- 458 Baltay, A., R. Abercrombie, S. Chu, and T. Taira (2024). The SCEC/USGS Community Stress Drop Validation Study Using the 2019
459 Ridgecrest Earthquake Sequence. *Seismica* **3**(1).
- 460 Beyreuther, M., R. Barsch, L. Krischer, T. Megies, Y. Behr, and J. Wassermann (2010). ObsPy: A Python toolbox for seismology [Software].
461 *Seismological Research Letters* **81**(3), 530–533.
- 462 Bindi, D., D. Spallarossa, M. Picozzi, and P. Morasca (2020). Reliability of source parameters for small events in central Italy: Insights
463 from spectral decomposition analysis applied to both synthetic and real data. *Bulletin of the Seismological Society of America* **110**(6),
464 3139–3157.
- 465 Bindi, D., D. Spallarossa, M. Picozzi, A. Oth, P. Morasca, and K. Mayeda (2023). The community stress-drop validation study—part II:
466 Uncertainties of the source parameters and stress drop analysis. *Seismological Society of America* **94**(4), 1992–2002.
- 467 Boatwright, J. (1978). Detailed spectral analysis of two small new york state earthquakes. *Bulletin of the Seismological Society of*
468 *America* **68**(4), 1117–1131.
- 469 Boatwright, J. (1980). A spectral theory for circular seismic sources; simple estimates of source dimension, dynamic stress drop, and
470 radiated seismic energy. *Bulletin of the Seismological Society of America* **70**(1), 1–27.
- 471 Boore, D. (1986). The effect of finite bandwidth on seismic scaling relationships. *Earthquake Source Mechanics* **37**, 275–283.
- 472 Boore, D. M. and W. B. Joyner (1997). Site amplifications for generic rock sites. *Bulletin of the seismological society of America* **87**(2),
473 327–341.
- 474 Brune, J. N. (1970). Tectonic stress and the spectra of seismic shear waves from earthquakes. *Journal of geophysical research* **75**(26),
475 4997–5009.
- 476 Campbell, K. W. and Y. Bozorgnia (2014). NGA-West2 ground motion model for the average horizontal components of PGA, PGV, and 5%
477 damped linear acceleration response spectra. *Earthquake Spectra* **30**(3), 1087–1115.
- 478 Castro, R., J. Anderson, and S. Singh (1990). Site response, attenuation and source spectra of S waves along the Guerrero, Mexico,
479 subduction zone. *Bulletin of the Seismological Society of America* **80**(6A), 1481–1503.
- 480 Chandler, A., N. Lam, and H. Tsang (2006). Near-surface attenuation modelling based on rock shear-wave velocity profile. *Soil Dynamics*
481 *and Earthquake Engineering* **26**(11), 1004–1014.
- 482 Chang, H., R. E. Abercrombie, N. Nakata, C. N. Pennington, K. B. Kemna, E. S. Cochran, and R. M. Harrington (2023). Quantifying
483 site effects and their influence on earthquake source parameter estimations using a dense array in Oklahoma. *Journal of Geophysical*
484 *Research: Solid Earth*, e2023JB027144.
- 485 Chang, H., Q. H., Z. Zhang, N. Nakata, and R. Abercrombie (2024). Investigation of site amplifications using ambient-noise-derived shallow
486 velocity structures under a dense array in Oklahoma. Manuscript submitted for publication.
- 487 Clouser, R. H. and C. A. Langston (1991). Qp-Qs relations in a sedimentary basin using converted phases. *Bulletin of the Seismological*
488 *Society of America* **81**(3), 733–750.

- 489 Cocco, M., E. Tinti, and A. Cirella (2016). On the scale dependence of earthquake stress drop. *Journal of Seismology* **20**, 1151–1170.
- 490 Cochran, E. S., A. Wickham-Piotrowski, K. B. Kemna, R. M. Harrington, S. L. Dougherty, and A. F. Peña Castro (2020). Minimal clustering
491 of injection-induced earthquakes observed with a large-n seismic array. *Bulletin of the Seismological Society of America* **110**(5), 2005–
492 2017.
- 493 Crain, K. D. and J. C. Chang (2018). Elevation map of the top of the crystalline basement in Oklahoma and surrounding states. *Oklahoma
494 Geol. Surv. Open-File Rept. OF1-2018*.
- 495 Dougherty, S. L., E. S. Cochran, and R. M. Harrington (2019). The Large-N seismic survey in Oklahoma (LASSO) experiment. *Seismological
496 Research Letters* **90**(5), 2051–2057.
- 497 Eshelby, J. D. (1957). The determination of the elastic field of an ellipsoidal inclusion, and related problems. *Proceedings of the royal society
498 of London. Series A. Mathematical and physical sciences* **241**(1226), 376–396.
- 499 Hanks, T. C. and H. Kanamori (1979). A moment magnitude scale. *Journal of Geophysical Research: Solid Earth* **84**(B5), 2348–2350.
- 500 Hartzell, S. H. (1978). Earthquake aftershocks as Green's functions. *Geophysical Research Letters* **5**(1), 1–4.
- 501 Hartzell, S. H. (1992). Site response estimation from earthquake data. *Bulletin of the Seismological Society of America* **82**(6), 2308–2327.
- 502 Heran, W. D., G. N. Green, and D. B. Stoeser (2003). A digital geologic map database for the state of Oklahoma. Technical report, U.S.
503 Geological Survey, Denver, CO.
- 504 Hough, S. (1997). Empirical Green's function analysis: Taking the next step. *Journal of Geophysical Research: Solid Earth* **102**(B3), 5369–
505 5384.
- 506 Hough, S. and J. Anderson (1988). High-frequency spectra observed at Anza, California: implications for Q structure. *Bulletin of the
507 Seismological Society of America* **78**(2), 692–707.
- 508 Johnson, K. S. and K. V. Luza (2008). *Earth sciences and mineral resources of Oklahoma*. Oklahoma Geological Survey.
- 509 Kemna, K., A. Peña Castro, R. Harrington, and E. S. Cochran (2020). Using a large-n seismic array to explore the robustness of spectral
510 estimations. *Geophysical Research Letters* **47**(21), e2020GL089342.
- 511 Kemna, K. B., A. Verdecchia, and R. M. Harrington (2021). Spatio-temporal evolution of earthquake static stress drop values in the 2016–
512 2017 central Italy seismic sequence. *Journal of Geophysical Research: Solid Earth* **126**(11), e2021JB022566.
- 513 Ko, Y.-T., B.-Y. Kuo, and S.-H. Hung (2012). Robust determination of earthquake source parameters and mantle attenuation. *Journal of
514 Geophysical Research: Solid Earth* **117**(B4).
- 515 Ktenidou, O., N. Abrahamson, R. Darragh, and W. Silva (2016). A methodology for the estimation of kappa (κ) from large datasets, example
516 application to rock sites in the NGA-East database, and implications on design motions. *PEER Report 2016* **1**.
- 517 Ktenidou, O.-J., N. A. Abrahamson, S. Drouet, and F. Cotton (2015). Understanding the physics of kappa (κ): Insights from a downhole
518 array. *Geophysical Journal International* **203**(1), 678–691.
- 519 Ktenidou, O.-J., F. Cotton, N. A. Abrahamson, and J. G. Anderson (2014). Taxonomy of κ : A review of definitions and estimation approaches
520 targeted to applications. *Seismological Research Letters* **85**(1), 135–146.
- 521 Laurendeau, A., F. Cotton, O.-J. Ktenidou, L.-F. Bonilla, and F. Hollender (2013). Rock and stiff-soil site amplification: Dependency on
522 v_{s30} and kappa (κ_0). *Bulletin of the Seismological Society of America* **103**(6), 3131–3148.
- 523 Madariaga, R. (1976). Dynamics of an expanding circular fault. *Bulletin of the Seismological Society of America* **66**(3), 639–666.

- 524 Mayeda, K., L. Malagnini, and W. R. Walter (2007). A new spectral ratio method using narrow band coda envelopes: Evidence for non-
525 self-similarity in the Hector Mine sequence. *Geophysical Research Letters* **34**(11).
- 526 Newville, M., T. Stensitzki, D. B. Allen, M. Rawlik, A. Ingargiola, and A. Nelson (2016). LMFIT: Non-linear least-square minimization and
527 curve-fitting for Python [Software]. *Astrophysics Source Code Library*, ascl-1606.
- 528 Oth, A., D. Bindi, S. Parolai, and D. Di Giacomo (2011). Spectral analysis of K-NET and KiK-net data in Japan, Part II: On attenuation
529 characteristics, source spectra, and site response of borehole and surface stations. *Bulletin of the Seismological Society of America* **101**(2),
530 667–687.
- 531 Oth, A., H. Miyake, and D. Bindi (2017). On the relation of earthquake stress drop and ground motion variability. *Journal of Geophysical
532 Research: Solid Earth* **122**(7), 5474–5492.
- 533 Parolai, S., C. G. Lai, I. Dreossi, O.-J. Ktenidou, and A. Yong (2022). A review of near-surface Q_S estimation methods using active and
534 passive sources. *Journal of Seismology* **26**(4), 823–862.
- 535 PEER (2015). NGA-East: Median ground-motion models for the Central and Eastern North America region (No.2015/04). Technical
536 report, Pacific Earthquake Engineering Research Center (PEER).
- 537 Rubinstein, J. L., W. L. Ellsworth, and S. L. Dougherty (2018). The 2013–2016 induced earthquakes in Harper and Sumner Counties,
538 southern Kansas. *Bulletin of the Seismological Society of America* **108**(2), 674–689.
- 539 Shearer, P. M., R. E. Abercrombie, D. T. Trugman, and W. Wang (2019). Comparing EGF methods for estimating corner frequency and
540 stress drop from P wave spectra. *Journal of Geophysical Research: Solid Earth* **124**(4), 3966–3986.
- 541 Shearer, P. M., G. A. Prieto, and E. Hauksson (2006). Comprehensive analysis of earthquake source spectra in southern California. *Journal
542 of Geophysical Research: Solid Earth* **111**(B6).
- 543 Supino, M., G. Festa, and A. Zollo (2019). A probabilistic method for the estimation of earthquake source parameters from spectral
544 inversion: application to the 2016–2017 Central Italy seismic sequence. *Geophysical Journal International* **218**(2), 988–1007.
- 545 U.S. Geological Survey. Earthquake Hazards Program Advanced National Seismic System (ANSS) Comprehensive Catalog of Earthquake
546 Events and Products: Catalog ($m > 3$) in Central Oklahoma (2016-04-14–2016-05-10) [data set]. Last accessed on 2022-09-19.
- 547 White, M. C., H. Fang, N. Nakata, and Y. Ben-Zion (2020). PyKonal: a Python package for solving the eikonal equation in spherical and
548 Cartesian coordinates using the fast marching method [Software]. *Seismological Research Letters* **91**(4), 2378–2389.
- 549 Winkler, K. W. and A. Nur (1982). Seismic attenuation: Effects of pore fluids and frictional-sliding. *Geophysics* **47**(1), 1–15.

550 **FULL MAILING ADDRESS FOR EACH AUTHOR**

- 551 • Hilary Chang: Department of Earth, Atmospheric, and Planetary Sciences,
552 Massachusetts Institute of Technology; 54-216, 77 Massachusetts, Cambridge, MA,
553 02139, USA

- Rachel E. Abercrombie: Department of Earth and Environment, Boston University;
685 Commonwealth Avenue, Room 130, Boston, MA, 02215, USA
 - Nori Nakata: Earth and Environmental Sciences Area, Lawrence Berkeley National Laboratory; 1 Cyclotron Rd, Berkeley, CA, 94720, USA

List of Figures

623	8	Apparent corner frequency (f_c) of the synthetic P-wave spectra of event L1 in synthetic test 2 – test 5 ((a) – (d)). (e) is the measured f_c from actual data in Kemna et al. (2020). Left: f_c vs the actual Q_{site} used to generate the spectra. Right: f_c vs the hypocentral distance. Red and blue dashed lines are the true f_c and the median of the mea- surements, respectively. The gray scales indicate fitting uncertainty ((standard deviation of f_c)/ f_c x 100%).	19
624			
625	9	Measured corner frequency (f_c) of event L1 in refit test 1. Left: f_c vs Q_{site} . Right: f_c vs hypocentral distance. We restrict to sites with higher Q_{site} values and hence there are fewer data points compared to Figure 8(e). The gray scales indicate fitting uncertainty ((standard deviation of f_c)/ f_c x 100%). The error bars indicate standard deviation. The blue dashed lines are the median f_c . Each point represents a subarray with 15 – 20 stations within a 2.5 km diameter circle.	22
626			
627	10	Apparent scaling relation between corner frequency (f_c) and moment magnitude (M_w) in (a) Kemna et al. (2020), (b) refit test 2, and (c) refit test 3. Each dot is the median of an event (among subarrays) with error bars indicating the standard deviation of f_c . The colors indicate the median Q_{site} of subarrays involved in the measurements. The black lines are constant stress drops at 1, 10, and 100 MPa. The shades indi- cate approximate upper bandwidth limits defined as one and two third of the maximum available frequency of the stacked spectra at subarrays.	22
628			
629			
630			
631			
632			
633			
634			
635			
636			
637			
638			
639			
640			
641			
642			
643			
644			
645			